Rough-Surface Polarimetry in Companion SAR Missions

Iannini, L.; Comite, D.; Pierdicca, N.; Lopez-Dekker, P.

Important note
To cite this publication, please use the final published version (if applicable).
Please check the document version above.

Rough-Surface Polarimetry in Companion SAR Missions

Lorenzo Iannini, *Member, IEEE*, Davide Comite, *Senior Member, IEEE*,
Nazzareno Pierdicca, *Senior Member, IEEE*, and Paco Lopez-Dekker, *Senior Member, IEEE*

Abstract—**Bistatic scattering from rough surfaces is typically
approached through the analysis of the scattered field in the
conventional H and V polarization basis, which coincides with
the zenith and azimuth unit vectors in a spherical reference
frame. This study delves into the impacts of different choices
of the transmit and receive linear basis on the performance and
design of a synthetic aperture radar (SAR) mission receive-only
companion. This article formalizes the rotation of the scattered
wave orientation at the antenna axes of the companion with
respect to the transmitted one and introduces a novel set of
linear polarizations, named principal polarizations, in transmit
and receive, deemed more suited to represent the scattering mech-
anisms of rough surfaces. Such a set is defined by the polarization
bases that maximize the radar cross section. It is shown that
the theoretical estimates from the proposed geometrical frame-
work provide a good agreement with analytical and numerical
simulations, performed considering state-of-the-art numerical
solutions. In addition, this article promotes the hypothesis that
a bistatic radar configuration, defined through the conventional
H and V linear basis, presents a strong similarity, from a target
information retrieval standpoint, to a monostatic compact φ-pol
mode, i.e., with the transmission of a linear polarization rotated
by an angle φ. The rotation φ varies over the swath and as
a function of satellite separation. For baselines of 250–300 km,
such as those envisioned by the European Space Agency (ESA)
Harmony Earth Explorer candidate, and for steep incidence
angles, an equivalent $\pi/8$-pol can be achieved for rough surfaces.**

Index Terms—**Bistatic scattering, compact polarizations, com-
panion synthetic aperture radar (SAR) missions, Earth explorer
harmony, rough-surface polarimetry, scattering symmetry.**

I. INTRODUCTION

UNDERSTANDING and modeling bistatic radar scattering
properties is gaining importance as an increasing number
of bistatic radar mission concepts are being considered for
implementation. The range includes bistatic radars that exploit
signals of opportunity, such as GNSS and communication
satellite signals [2]–[4], which operate by collecting the
quasi-specular reflections [5], and, most relevantly for the
present study, companions for synthetic aperture radar (SAR)

missions, only limitedly diverging from the backscatter con-
cept characteristics. The technological readiness of bistatic
radars operation (or, more generally, multistatic) has been
demonstrated by the TanDEM-X mission [6]. However, from a
theoretical viewpoint, TanDEM-X and similar concepts, such
as the proposed Tandem-L [7] mission, due to the short
distance between the spacecrafts defining the bistatic config-
uration, can be considered as quasi-monostatic. In contrast,
recent concepts, e.g., the SAOCOM companion satellite [8],
the SESAME mission proposal [9], or Harmony (currently
the only remaining ESA Earth Explorer 10 candidate [10]),
assume geometries with long baselines, defining therefore
significant bistatic angles (namely, larger than 20°) [9], [11].

Increasing bistatic angles lead to changing the electromag-
netic scattering mechanisms and, thus, the radar polarimetric
signature. As a matter of fact, scattering mechanisms that can
be dominant in a monostatic geometry, such as scattering off
dihedrals or trihedrals, need to be revisited when operating in
bistatic configurations. The complexity of bistatic polarime-
try is also related to the higher degree of freedom of its
geometry [12]–[15]. In monostatic polarimetry, a rotation of
the target about the line of sight is equivalent, in terms of
polarimetric response, to the same rotation of the antenna
plane in the opposite direction. This makes the target response
roll invariant. Various symmetry properties for the polarimetric
scattering features have been demonstrated in the presence of
symmetry groups for the scene [16].

Monostatic radar polarimetry is an established paradigm
with some well-defined conventions. Conversely, in bistatic
polarimetry, the nature of the mechanisms can be more com-
plicated and depends on the following factors: 1) the target
orientation with respect to the receiver and transmitter line
of sights, 2) the orientation of the polarization unit vectors,
and 3) the baseline between the two antennas. An immedi-
ate effect of these features is the loss of polarimetric reci-
procity. This can add additional degrees of freedom to the
form of the covariance/coherence matrix describing distributed
targets.

The most general polarization of the electromagnetic wave
impinging on (or scattered from) a surface can be described as
linear combinations of a vertical (V) field component (parallel
to the incidence plane, oscillating within the plane normal to
the surface) and a horizontal component (H), orthogonal to the
incidence plane, oscillating in a plane parallel to the surface.
Dealing with the normalized radar cross section (NRCS) of a

target, the combination of transmit and receive polarizations is typically specified as σ_0^{qp}, where the second superscript, p, indicates the polarization of the transmitted signal (or antenna) and the first, q, the polarization of the receiving antenna.

In the monostatic case, an H–V polarization basis is convenient because the scattering mechanisms can often be well-described in terms of these polarizations. For natural surfaces, the cross-polar NRCS in an H–V basis is typically very small [11], [17], i.e., $\sigma_0^{hv} \approx 0$ and the polarization ratio PR $= \sigma_0^{vv}/\sigma_0^{hh}$, and polarization difference PD $= \sigma_0^{vv} - \sigma_0^{hh}$, can have relatively straightforward geophysical meaning (e.g., PR>1 for Bragg scattering).

The bistatic literature often holds the H–V convention [11], [17], [18]. However, as polarization is defined in a plane orthogonal to the propagation direction, the scattered and incident polarizations do not have the same orientation. Therefore, it is convenient to refer to unit vectors $\hat{h}_i$ and $\hat{v}_i$ for the incident H and V polarizations and to $\hat{h}_s$ and $\hat{v}_s$ for the H and V polarizations of the received signal. For example, in a bistatic geometry, σ_0^{hv} can be large compared with σ_0^{vv}, but this can be a direct consequence of the measurement geometry and may not have any geophysical implication or intrinsic informational value [11]. The bistatic geometry, indeed, determines a rotation of the orientation of the scattered field related to the bistatic azimuth angle between the two antennas, i.e., Ω in Fig. 1. It occurs, for instance, that a signal transmitted in V is predominantly received in H for $\Omega = \pi/2$ [18]. A polarization rotation of approximately $\pi/2$ would be hence experienced without any implication about depolarization phenomena. The bistatic spaceborne case in Fig. 1 reports a typical along-track (AT) baseline companion scenario (with transmitter and receiver at 400 km), where the bistatic azimuth angle is in the order of 40°. These rotations of the polarization are not experienced in monostatic radars: assuming a V-polarized wave in transmission, the V- and H-polarized signals in most cases represent the strongest and the weakest NRCS, respectively.

From an application viewpoint, it is desirable to define sets of polarization basis that facilitate the geophysical interpretation of data. To do this, it is important to make the vector nature of the polarization state explicit. This article is therefore aimed at addressing the following aspects:

1) defining a linear principal polarization basis for rough-surface bistatic polarimetry. This set, composed of the principal transmit polarization (PTP) and the principal receive polarization (PRP) at the two antennas, is related to the geometry of the radar system. As graphically conveyed by Fig. 1, it corresponds to the set that registers the maximum scattered intensity.

2) quantifying the rotation of the polarization orientation for a generic linear transmit basis and assessing the possibility of treating bistatic geometries as a monostatic pseudo-compact equivalent from a polarimetric viewpoint.

3) determining the impact of the antenna polarization choices for companion missions on the NRCS and on the polarimetric sensitivity to rough-surface characteristics.

The assessment of these propositions relies on simulations performed exploiting different numerical methods: the first-order Kirchoff approximation (KA) technique, the second-order method from Elfouhaily in [1], the second-order small-slope approximation (SSA2) [17], and the full-wave numerical solution based on a method of moments (MoM) approach. Note that the analysis is carried out on perfect electric conductors (PECs). Consequently, the conclusions that are drawn will be applicable with a good degree of confidence mainly to water surfaces.

This work is developed in the framework of the ESA Earth Explorer Harmony mission, which is based on the use of two receive-only radar satellites operating as companions of one of the ESA Sentinel-1 (S1) missions [19]. Harmony will fly on approximately the same orbital plane as S1, at an AT distance in the range of 200–400 km, either with the two Harmony spacecrafts flying in close formation to form a single-pass interferometer or with one spacecraft leading and the other trailing S1, in a so-called StereoSAR formation.

II. THEORETICAL BACKGROUND

Let us consider the right-handed system of coordinates (x, y, z) shown in Fig. 1, with unit vectors $(\hat{x}, \hat{y}, \hat{z})$ and a rough surface $h(x, y)$ characterized by an average height $\langle h \rangle = 0$ and local surface normals $\hat{n}$. For a canonical radar scenario, the upper half-space medium consists of free air where waves propagate with wavenumbers $k = 2\pi f_0$, whereas the lower half-space medium is a dielectric. The incident and scattered waves propagate along the vectors $\vec{k}_i = k\hat{i}$ and $\vec{k}_s = k\hat{s}$, where k is the wavenumber and $\hat{i}$ and $\hat{s}$ are the unit vectors, both directed toward the target, as dictated by the backscattering alignment (BSA) convention. The convenience of BSA for companion missions with small bistatic angles is the consistency of the horizontal polarization sign with the one commonly adopted for monostatic configurations. The incident direction $\hat{i} = i_x\hat{x} + i_y\hat{y} + i_z\hat{z}$ can be expressed as

$$\begin{cases} i_x = 0 \\ i_y = \sin\theta_i \\ i_z = -\cos\theta_i \end{cases} \tag{1}$$

where θ_i stands for the incidence angle. Note that the plane of incidence, i.e., the plane formed by $\hat{i}$ and $\hat{z}$, has been arbitrarily aligned to $\hat{y}$, with no loss of generality for isotropic surfaces. Similarly, the scattered field for the zenith observation angle θ_s and for the azimuth bistatic angle Ω is characterized by $\vec{k}_s = k\hat{s}$ with $\hat{s} = s_x\hat{x} + s_y\hat{y} + s_z\hat{z}$ and

$$\begin{cases} s_x = -\sin\Omega \sin\theta_s \\ s_y = \cos\Omega \sin\theta_s \\ s_z = -\cos\theta_s \end{cases} \tag{2}$$

where, in accordance with Fig. 1, Ω is defined as the counterclockwise angle with respect to the negative y axis. The specular and backscatter configurations are then represented by $\theta_s = \theta_i$ with $\Omega = 0$ and $\Omega = \pi$, respectively. Bistatic angles $\Omega \neq 0, \pi$ denote out-of-plane scattering.

The incident plane wave can then be defined by

$$\vec{E}^i = \hat{p}E_0 e^{-j\vec{k}_i \cdot \vec{r}} = \hat{p}E^i \tag{3}$$

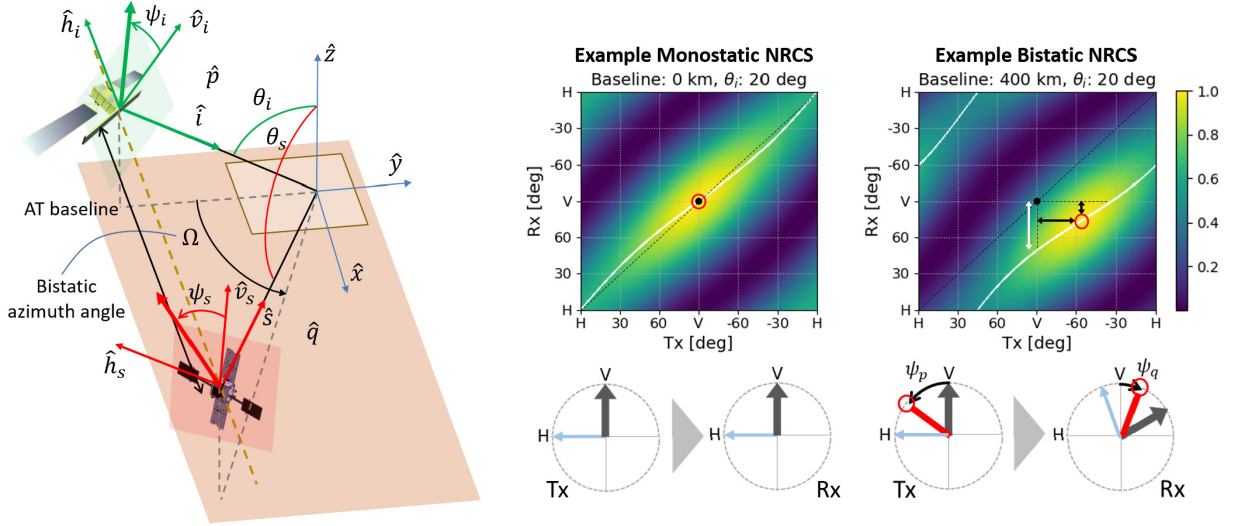$$\vec{H}^i = \hat{i} \times (\hat{p}E^i)/\eta \tag{4}$$

Fig. 1. (Left Panel) Essential geometry of a bistatic companion satellite mission, with a "passive" receiver (in red) collecting the scattered signal generated by an "active" radar (in green). (Right Panel) monostatic and bistatic polarization behavior examples. For each configuration, the NRCS from a rough surface, computed through the approach in [1], is shown for all possible combinations of linear transmit and receive polarization orientations. The NRCS is normalized by the maximum value, i.e., for the principal polarization, labeled with a red circle. The vertical span between the white curve and the dashed black line represents the orientation rotation.

where the unit vector $\hat{p}$, orthogonal to $\vec{k}_i$, defines a generic polarization in the 3-D space and η is the wave impedance. The scattered field in the far zone is a function of the tangential fields on the rough surface, $\hat{n} \times \vec{E}$ and $\hat{n} \times \vec{H}$, and can be derived through the Stratton–Chu integrals as

$$E_{qp}^s = \frac{jk}{4\pi R} e^{-jkR} \hat{q} \cdot \int \left[\hat{k}_s \times \left(\hat{n} \times \vec{E} \right) + \eta \left(\hat{n} \times \vec{H} \right) \right] e^{j\vec{k}_s \cdot \vec{r}} ds \tag{5}$$

where $\hat{q}$, orthogonal to $\vec{k}_s$, denotes the polarization for which the scattered field is calculated, and R is the distance of the receiver. The signs are adjusted coherently with the direction of $\vec{k}_s$, which points toward the target. The full expression of the tangential fields $\hat{n} \times \vec{E}$ and $\hat{n} \times \vec{H}$ can be found in Poggio and Miller [20].

A rigorous solution demands complex numerical calculations depending on the wavelength and surface roughness. At the current moment, no compact closed-form solutions exist for a generic dielectric. The problem can be more easily tackled for PECs, which effectively mimic the behavior of high-permittivity media, such as water. It is important to premise that hereafter the investigation will focus on PEC models, and therefore its conclusions will be mainly drawn for ocean surfaces.

Note that we are not interested in the radiometric component of rough surface scattering, but rather on polarimetric behavior. Therefore, in the rephrased scattered field expression

$$\vec{E}^s = \vec{P}(\hat{p}) \cdot C \tag{6}$$

the focus shall be on the second-order behavior of vector P rather than on radiometric factor C, which is not polarization-dependent. This article will leverage on the existing approaches in literature to cover this part. An interesting derivation is the one debated by Elfouhaily *et al.* in [1] for PEC, which leads to the relatively simple analytic expression

$$\vec{P} = \vec{P}_1 + \vec{P}_{\text{sup}} \tag{7}$$

where

$$\vec{P}_1 \propto -\hat{s} \times \left(\vec{k}_{s,i} \times \left(\hat{p} \times \hat{i} \right) \right) \times \hat{s} \tag{8}$$

and

$$\vec{P}_{\text{sup}} \propto -\hat{s} \times \left\{ 2 \left(\vec{k}_H \cdot \vec{p}_H \right) \vec{K}_H - \left(\vec{k}_H \cdot \vec{K}_H \right) \vec{p}_H \right\} \times \hat{s} \tag{9}$$

stand as the contributions from the first-order approximation and from the higher order scattering terms, respectively. In (8), $\vec{k}_{i,s}$ is the bisector of the transmitter–target–receiver angle

$$\vec{k}_{i,s} = \vec{k}_s + \vec{k}_i \tag{10}$$

and $k_z = \vec{k}_{i,s} \cdot \hat{z}$. For the supplemental field in (9), the horizontal vectors $\vec{p}_H = \hat{z} \times (\hat{p} \times \hat{i})$, $\vec{k}_H = \hat{z} \times \vec{k}_{s,i} \times \hat{z}$, and $\vec{K}_H = (1/2)((\hat{z} \times \hat{i} \times \hat{z} / \cos\theta_i) - (\hat{z} \times \hat{s} \times \hat{z} / \cos\theta_s))$ are introduced. The field $\vec{P}_1$ is derived from the tangent plane approximation, and hence it represents KA. Although its compactness makes it a convenient tool for approaching analytically the polarization rotation problem, the tangent plane approximation constrains the validity region of the KA approach to surfaces with large curvatures. To have more accurate intensity and rotation estimates, the second-order scattering term in $\vec{P}_{\text{sup}}$ shall also be accounted for.

The interaction of the wave with the surface introduces a rotation in the polarization orientation, herewith referred to as "polarization rotation," depending on the transmitter and receiver angles. The rotation is readily defined as

$$\triangle\psi = \psi_s - \psi_i \tag{11}$$

with ψ_i and ψ_s standing for the polarization orientation of the incidence and scattered fields. The orientation shall be computed with respect to a reference linear polarization basis. As illustrated in Fig. 1, in this work, the angle will be referred to the conventional right-handed (h, v) set. For a generic electric field, it can be derived through [21]

$$\psi = \frac{1}{2} \arctan\left(\frac{2\mathcal{R}(C_x)}{C_v - C_h} \right) \tag{12}$$
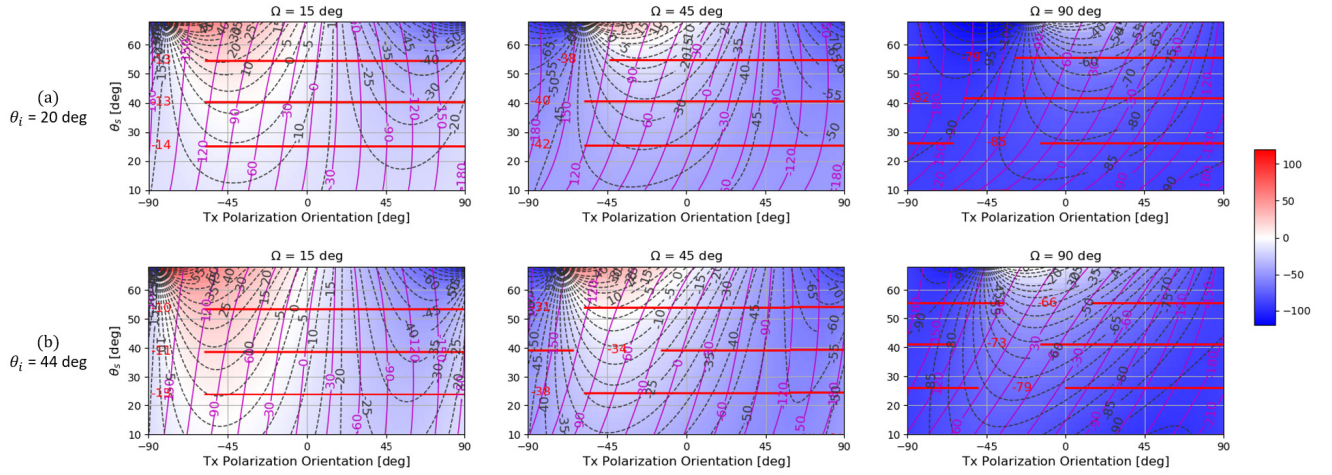
Fig. 2. Polarization rotations experienced by the received field for different orientations ψ_i of the transmit polarization, zenith observation angles θ_s, and bistatic azimuth angles Ω (15°, 45°, and 90°). The values are reported for the two incidence angles θ_i of (a) 20° and (b) 44°. In each panel, the background images and the gray contour lines refer to the second-order Elfouhaily model $\bar{P}$ in (7), the red contour lines to $\bar{P}_1$ in (8), and the magenta lines to the supplementary field $\bar{P}_{\text{sup}}$ in (9). The orientation $\psi_i = 0$ represents the nominal V.

where C_h, C_v, and C_x express the copol and cross-pol second-order field statistics

$$\begin{bmatrix} C_v & C_x^* \\ C_x & C_h \end{bmatrix} = \begin{bmatrix} \langle E_v E_v^* \rangle & \langle E_v E_h^* \rangle \\ \langle E_h E_v^* \rangle & \langle E_h E_h^* \rangle \end{bmatrix} \quad (13)$$

with the $\langle . \rangle$ operator representing the ensemble average. In the case of deterministic expression of the field vector $\vec{E}$, such as for $\hat{p}$ and $\vec{P}$, the more straightforward derivation $\psi = \arctan(E_h/E_v)$ can be used. Note that ψ can cover the range $(-\pi/2, \pi/2)$ by accounting for the sign of $\mathcal{R}(C_x)$. According to such notation, the horizontal and vertical polarizations are characterized by $\psi_h = \pi/2$ and $\psi_v = 0$, respectively.

Besides varying with the illumination geometry, the rotation is also dependent on the transmit orientation ψ_i. As conveyed in Fig. 2, the first KA and the higher order field components have a notably different behavior. For a given incidence and bistatic angle, the KA component has no sensitivity to the polarization orientation and has weak sensitivity to the zenith scattering angle θ_s. Conversely, the supplementary component is more sensitive than the KA component to θ_s and, most interestingly, it has fast rotation variations with ψ_i, covering the whole 2π range of rotation angles. The most relevant aspect is that, for any given geometry, it is possible to find 1) a polarization orientation for which the two components sum constructively and 2) a second polarization for which the two fields interact in a destructive way. This effect has many practical implications on radiometry and is in fact directly related to the concept of principal polarizations, which will be further elaborated in Section IV. A further consequence for small bistatic angles (including the monostatic configuration) is that of making the magnitude of field transmitted in V larger than the one of the field transmitted in H, confirming a well-known property for sea surfaces.

III. POLARIMETRY AND SCENE SYMMETRIES

When two polarizations are available in transmit (quad-pol systems), the full second-order characterization of an incoherent target can be arranged into the 4×4 covariance matrix [16], [22]

$$\mathbf{C} = \langle \mathbf{s} \cdot \mathbf{s}^H \rangle \quad (14)$$

where $\mathbf{s} = \begin{bmatrix} S_{hh} & S_{vh} & S_{hv} & S_{vv} \end{bmatrix}^T$ is the vectorized Sinclair scattering matrix and the superscript H indicates the conjugate transpose operator. In its most generic expression, the matrix counts 16 real-valued independent parameters: four real-valued variances (or intensities) and six complex-valued covariances. Depending on the target geometry and the antenna orientations, some elements of the covariance matrix carry on redundant information. For instance, for azimuthally isotropic rough surfaces and in monostatic configuration, in addition to the reciprocity condition (i.e., $S_{hv} = S_{vh}$), the reflection symmetry property holds, namely, $\langle S_{hh} S_{hv}^* \rangle = \langle S_{vv} S_{hv}^* \rangle = 0$ [23].

In those conditions, the covariance of a monostatic system can then be written as

$$\mathbf{C}^{(m)} = \mathbf{C}\left(\vec{k}_i = \vec{k}_s\right)$$

$$= \begin{bmatrix} \sigma_{hh}^{(m)} & 0 & 0 & \rho^* \sqrt{\sigma_{hh}^{(m)} \sigma_{vv}^{(m)}} \\ 0 & \sigma_{hv}^{(m)} & \sigma_{hv}^{(m)} & 0 \\ 0 & \sigma_{hv}^{(m)} & \sigma_{hv}^{(m)} & 0 \\ \rho \sqrt{\sigma_{hh}^{(m)} \sigma_{vv}^{(m)}} & 0 & 0 & \sigma_{vv}^{(m)} \end{bmatrix} \quad (15)$$

with σ_{ij} standing for $\langle S_{ij} S_{ij}^* \rangle$, ρ indicating the correlation coefficient (coherence) between S_{hh} and S_{vv}, and the superscript (m) recalling the monostatic condition. Note that the matrix can be compacted into a 3 x 3 format; however, we reported the full version to remain consistent with the bistatic expression hereafter used, lacking in the reciprocity and the reflection symmetry properties.

For bistatic geometries, the conventional (h, v) linear polarization bases are not aligned with the plane formed by $\hat{i}$ and $\hat{s}$, typically referred to as scattering plane. This section introduces a polarization set (h', v') which is matched to the scattering
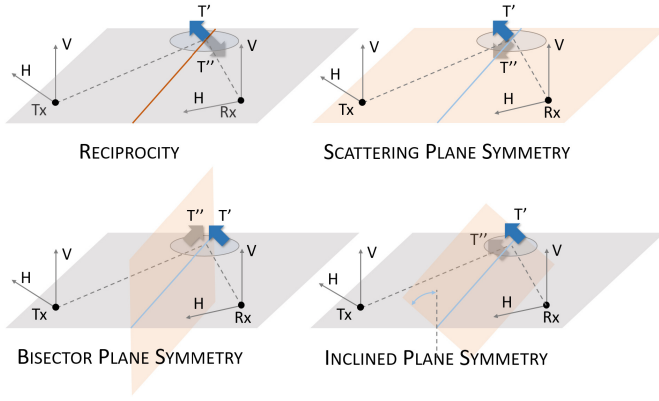
Fig. 3. Symmetries in a bistatic scattering problem. The line and planes of symmetry are highlighted with red color. The scattering plane and the bisector are otherwise represented, respectively, by a gray plane and a blue line. The original (T') and adjoint (T'') scatterers are symbolically illustrated with arrows. The first three symmetries introduce mathematical constraints to the scattering problem, whereas a symmetry with respect to an arbitrary plane (bottom right plot) does not lead to any general scattering property.

plane and will elaborate on its relevance in specular scattering and in the symmetry properties for distributed targets. It shall be premised that this coordinate set does not consist in the so-called principal polarizations for rough surfaces. Its role within this article is to provide a significant insight on the specular part of the scattered field.

In satellite systems, the horizontal and vertical polarization orientations are typically determined by aligning the horizontal antenna axis to the ground surface, assumed flat, i.e., orthogonal to $\hat{z}$. By extension, this choice is also commonly adopted for bistatic configurations, assuming that both the active and passive antennas comply with the ground alignment. The horizontal polarization versors are given by

$$\hat{h}_i = \frac{\hat{z} \times \hat{i}}{|\hat{z} \times \hat{i}|}, \quad \hat{h}_s = \frac{\hat{z} \times \hat{i}}{|\hat{z} \times \hat{i}|}. \tag{16}$$

According to BSA convention, the vertical polarizations can be readily derived through

$$\hat{v}_i = \hat{i} \times \hat{h}_i, \quad \hat{v}_s = \hat{s} \times \hat{h}_s. \tag{17}$$

A different polarization basis has also been proposed, enforcing an alignment with the scattering plane [14], [24], [25]. In this case, the horizontal polarization unit vectors, $\hat{h}'$, lie on the scattering plane and the vertical polarization unit vectors, $\hat{v}'$, are consequently orthogonal to it. In formulas

$$\hat{v}' = \hat{v}'_i = \hat{v}'_s = \frac{\hat{i} \times \hat{s}}{|\hat{i} \times \hat{s}|} \tag{18}$$

$$\hat{h}'_i = \hat{v}' \times \hat{i}, \quad \hat{h}'_s = \hat{v}' \times \hat{s}. \tag{19}$$

The main relevance of this rotated set lies in its invariance for specular scattering, as detailed in Appendix A, and in its central role in the symmetry properties. To discuss these latter, we further introduce the plane that the bisector describes with $\hat{v}'$, and hence orthogonal to the scattering plane, which will be referred to as bisector plane. As illustrated in Fig. 3, the three types of symmetry scenarios can now be addressed [24]:

1) *Reciprocity*, characterized by scattering invariance to rotations of the scene of π about the bisector

2) *Scattering plane symmetry*, characterized by scattering invariance to mirroring the scene with respect to the scattering plane
3) *Bisector plane symmetry*, characterized by scattering invariance to mirroring the scene with respect to the bisector plane.

For coherent targets, the reciprocity condition determines the equivalence of the cross-polarized returns in the base $(\hat{h}', \hat{v}')$, i.e., $S_{h'v'} = S_{v'h'}$, whereas for incoherent targets it leads to second-order expressions discussed in Appendix A (see 49). It is important to clarify that with *reciprocity* we do not refer to antenna/scattering reciprocity theorem, responsible for (42) and (43). This latter is always valid although it is not sufficient to ensure the cross-polarized ($h'v'$ and $v'h'$) channel equivalence in a bistatic geometry.

The combination of target reciprocity with one of the two mirroring symmetries then leads to a complete decorrelation between the cross-polarized and copolarized components, and therefore to the same covariance expression as in (15). The reader is referred to Appendix A for an explicit derivation of the scattering properties associated with the presence of a bisector plane symmetry and to reciprocity. It should be, however, considered that the occurrence of reciprocity conditions in bistatic configurations is rare.

Random surfaces with azimuth isotropy shall be rather regarded as potentially symmetric targets, as they are characterized by an infinite set of symmetry planes passing through the mean surface normal $\hat{n}_s$, assumed here to correspond to the vertical axis $\hat{z}$. Among these, the plane formed by $\hat{z}$ with the bisector in (10), represented in blue in Fig. 4, is of particular interest. A mirroring symmetry would apply to rough surfaces for a limited set of observation angles, most notably for $\theta_s = \theta_i$. Such scenario would be characterized by the relationships in (46), and the full covariance matrix would take the form

$$\mathbf{C}_{h',v'}\left(\vec{k}_i, \vec{k}_s\right) = \begin{bmatrix} \sigma_{h'h'}^{(b)} & \epsilon_{xv'}^* & -\epsilon_{xh'}^* & c_{co}^{(b)*} \\ \epsilon_{xh'} & \sigma_{h'v'}^{(b)} & c_x^{(b)} & \epsilon_{xv'}^* \\ -\epsilon_{xh'} & c_x^{(b)} & \sigma_{v'h'}^{(b)} & -\epsilon_{xv'}^* \\ c_{co}^{(b)} & \epsilon_{xv'} & -\epsilon_{xv'} & c_{v'v'}^{(b)} \end{bmatrix} \tag{20}$$

where

$$\sigma_{ij}^{(b)} = \left\langle S_{ij} S_{ij}^* \right\rangle$$
$$c_x^{(b)} = \left\langle S_{v'h'} S_{h'v'}^* \right\rangle$$
$$c_{co}^{(b)} = \rho^{(b)} \sqrt{\sigma_{h'h'} \sigma_{v'v'}}$$
$$\epsilon_{xh'} = \left\langle S_{h'v'} S_{h'h'}^* \right\rangle$$
$$\epsilon_{xv'} = \left\langle S_{v'v'} S_{h'h'}^* \right\rangle.$$

It can be observed that without reciprocity, the matrix is full. Nevertheless, for small baselines, low values are expected for $\epsilon_{xv'}$ and $\epsilon_{xv'}$, when compared with the intensity of the copolarized channels. It is important to emphasize that the (h', v') basis is the one that minimizes the leakages in ϵ since v' is aligned to the bisector symmetry plane. It should also be remarked that companion missions are not in the $\theta_s = \theta_i$ configuration. In a generic bistatic geometry (e.g., the two
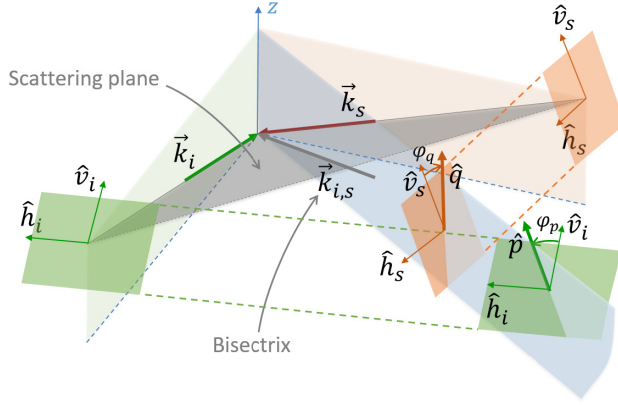
Fig. 4. Schematic representation of the bistatic illumination geometry, including the transmit and receive antenna planes (light green and light orange colors, respectively) with their horizontal and vertical polarization unit vectors ($\hat{h}$ and $\hat{v}$), the incident and scattering wave vectors, forming the scattering plane (gray color), and the symmetry plane (light blue color) here defined as the plane formed by the zenith versor ($\hat{z}$) and the bisector $\vec{k}_{i,s}$. Note that the bisector plane is not depicted for clarity.

systems placed at different heights), the symmetry plane is inclined with respect to the bisector plane (which we remind being defined by $\hat{v}'$ and (10)). In Fig. 3, this scenario is represented by the last panel. Such generic symmetry plane scenario does not introduce additional constraints. Nevertheless, in Section IV, we postulate that the reflection symmetry conditions can roughly apply to rough surfaces upon a proper basis rotation.

IV. PRINCIPAL POLARIZATIONS

In this article, we introduce a novel set of linear polarizations, named principal transmit and receive polarization (PTP and PRP) and expressed in the (h, v) basis as

$$\text{PTP}_m : \mathbf{p}_m = \begin{bmatrix} \cos\varphi_p \\ \sin\varphi_p \end{bmatrix}, \quad \text{PTP}_M : \mathbf{p}_M = \begin{bmatrix} -\sin\varphi_p \\ \cos\varphi_p \end{bmatrix} \quad (21)$$

$$\text{PRP}_m : \mathbf{q}_m = \begin{bmatrix} \cos\varphi_q \\ \sin\varphi_q \end{bmatrix}, \quad \text{PRP}_M : \mathbf{q}_M = \begin{bmatrix} -\sin\varphi_q \\ \cos\varphi_q \end{bmatrix} \quad (22)$$

hence defined by the characteristic rotation angles φ_p and φ_q, which lead to the scattering matrix in the new basis

$$\mathbf{S}_{qp} = \begin{bmatrix} S_{q_m p_m} & S_{q_m p_M} \\ S_{q_M p_m} & S_{q_M p_M} \end{bmatrix} = \mathbf{R}\left(-\varphi_q\right) \cdot \mathbf{S} \cdot \mathbf{R}\left(\varphi_p\right) \quad (23)$$

where $\mathbf{R}$ is the rotation matrix [15]

$$\mathbf{R}(\varphi_j) = \begin{bmatrix} \cos\varphi_j & \sin\varphi_j \\ -\sin\varphi_j & \cos\varphi_j \end{bmatrix} \quad (24)$$

and with $j = \{p, q\}$. The subscripts m and M refer to the minor and major polarization pairs, respectively. Supported by the visual example in Fig. 1, we define the major polarization pair, $\mathbf{p}_M$ and $\mathbf{q}_M$, as the unit vectors achieving the maximum NRCS, according to the expression

$$(\mathbf{p}_M, \mathbf{q}_M) = \underset{\mathbf{p}, \mathbf{q}}{\arg\max} \left(\mathbf{p}^T \otimes \mathbf{q}^T\right) \mathbf{C}(\mathbf{p} \otimes \mathbf{q}). \quad (25)$$

Note that an exact and compact mathematical solution to such maximization is cumbersome and possibly not largely

beneficial to the physical understanding of the problem. The approach advanced by this article has therefore a different nature. We postulate that such polarization can be related to the dominant scatterers' orientation, which lies on the symmetry plane of the surface passing through the bisector. The rationale follows from the expression of the covariance in (20) and from the hypothesis that the optimal set from a scattered magnitude perspective is indeed also the one that minimizes its off-diagonal elements. With the aid of Fig. 4, we can then further express φ_p and φ_q as the antenna axes rotations that provide the alignment between the nominal $\hat{v}$ and the symmetry plane. These angles are implicitly derived through

$$|\varphi_p| = \cos^{-1}(\hat{v}_i \cdot \hat{p}_M) \quad (26)$$

$$|\varphi_q| = \cos^{-1}(\hat{v}_s \cdot \hat{q}_M) \quad (27)$$

where the unit vectors for the major PTP and PRP take the expression

$$\hat{p}_M = \frac{(\vec{k}_{i,s} \times \hat{z}) \times \vec{k}_i}{\left|(\vec{k}_{i,s} \times \hat{z}) \times \vec{k}_i\right|}, \quad \hat{q}_M = \frac{(\vec{k}_{i,s} \times \hat{z}) \times \vec{k}_s}{\left|(\vec{k}_{i,s} \times \hat{z}) \times \vec{k}_s\right|}. \quad (28)$$

In the monostatic configuration, φ_p and φ_q are equal to 0, and the principal polarizations simply correspond to the horizontal and vertical polarizations. In particular, the minor principal set $\text{PTP}_m - \text{PRP}_m$ would correspond to the lowest backscattering polarization, hence to H, and the major one, $\text{PTP}_M - \text{PRP}_M$, would then correspond to V. In a generic geometry, under the assumption of (25), the axes' rotations φ_p and φ_q are equivalent to the polarization orientations of the major set $\text{PTP}_M - \text{PRP}_M$, i.e., $\psi_{p_M} = \varphi_p$ and $\psi_{q_M} = \varphi_q$. Consequently, the minor set $\text{PTP}_m - \text{PRP}_m$ is described by $\psi_{p_m} = \varphi_p + \pi/2$ and $\psi_{q_m} = \varphi_q + \pi/2$. Referring to (11), the polarization rotation experienced by PTP_m and PTP_M is readily expressed as

$$\Delta\psi_{p_m} = \Delta\psi_{p_M} = \varphi_q - \varphi_p. \quad (29)$$

The PTP and PRP orientations are illustrated in Fig. 5 for the two incidence angles of 20° and 44°. Note that the figure also provides a first empirical assessment through cross-comparison with the optimum for (25) from the Elfouhaily model. The panels convey that the two models provide a good match for the whole range of bistatic angles Ω, especially for the PTP, with discrepancies larger than 2° only for θ_s above 50°. The PRP accuracy presents a similar sensitivity to the zenith scattering angles, although with slightly worse adherence. The panels also convey that the principal polarizations are significantly different from the scattering plane polarizations (h', v'). As expected, the two sets coincide only for $\theta_s = \theta_i$.

The rationale of the alignment with the symmetry plane is that the sets (p_m, p_M) and (q_m, q_M) provide the best approximation to the covariance matrix of a symmetric and reciprocal target (see 50), hence leading to

$$\mathbf{C}_{\varphi_p, \varphi_q}\left(\vec{k}_i, \vec{k}_s\right) = \left(\mathbf{R}\left(-\varphi_p\right) \otimes \mathbf{R}\left(-\varphi_q\right)\right)$$
$$\cdot \mathbf{C}\left(\vec{k}_i, \vec{k}_s\right) \cdot \left(\mathbf{R}\left(\varphi_p\right) \otimes \mathbf{R}\left(\varphi_q\right)\right) \quad (30)$$

θ_i = 20 deg

PTP Orientation ψ_p [deg]

PRP Orientation ψ_q [deg]

θ_i = 44 deg

PTP Orientation ψ_p [deg]

PRP Orientation ψ_q [deg]

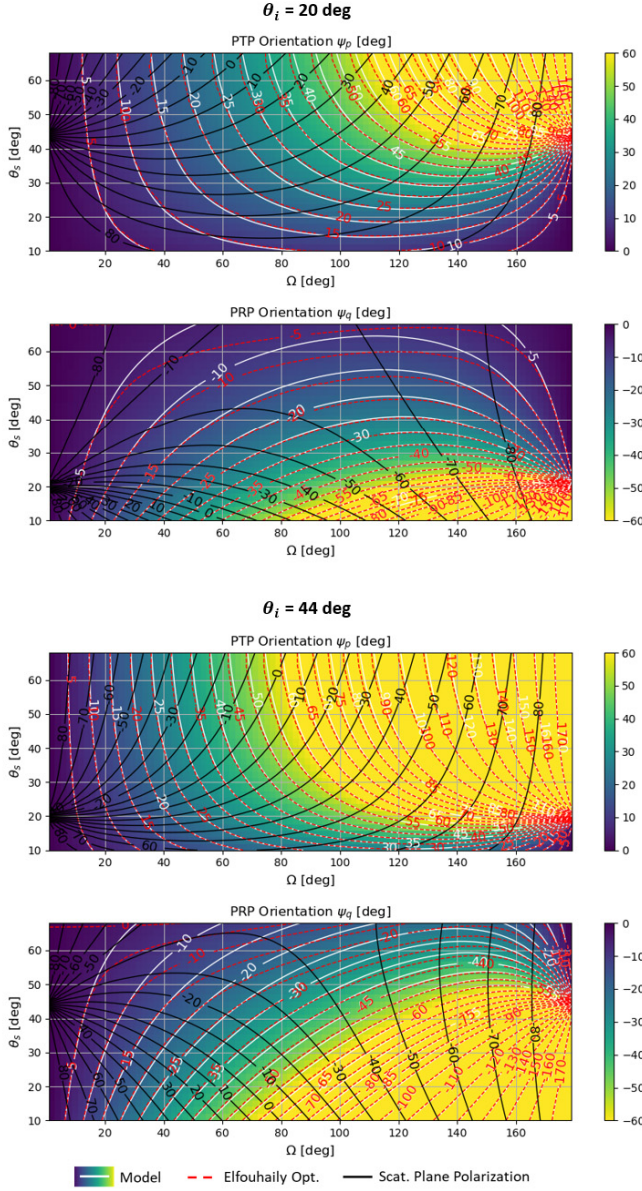Model — Elfouhaily Opt. — Scat. Plane Polarization

Fig. 5. Principal polarization orientations in transmit and receive for the two incidence angles of 20° (upper panels) and 44° (bottom panels). For cross-validation purposes, the solutions of (25) according to the second-order Elfouhaily model in (7) are reported (red-dashed contour lines). The scattering plane polarizations $\hat{v}_i'$ in transmit and $\hat{v}_s'$ in receive are also illustrated (black contour lines).

$$\cong \begin{bmatrix} \sigma_{q_m p_m}^{(b)} & 0 & 0 & c_{co}^{(b)*} \\ 0 & \sigma_{q_m p_M}^{(b)} & c_x^{(b)*} & 0 \\ 0 & c_x^{(b)} & \sigma_{q_M p_m}^{(b)} & 0 \\ c_{co}^{(b)} & 0 & 0 & \sigma_{q_M p_M}^{(b)} \end{bmatrix} \quad (31)$$

with

$$\sigma_{ij}^{(b)} = \left\langle S_{ij} S_{ij}^* \right\rangle$$
$$c_x^{(b)} = \left\langle S_{q_M p_m} S_{q_m p_M}^* \right\rangle$$
$$c_{co}^{(b)} = \rho^{(b)} \sqrt{\sigma_{q_m p_m}^{(b)} \sigma_{q_M p_M}^{(b)}}$$

and assuming

$$\left| \left\langle S_{q_l p_m} S_{q_i p_i}^* \right\rangle \right| \ll \sigma_{q_i p_i}^{(b)}, \quad \text{for } l \neq m$$

where $j, i, l, m = \{m, M\}$, $\otimes$ indicates the Kronecker product. Intuitively, the bistatic covariances can be parametrized and exploited in a similar way as in the monostatic geometry of (15) if the two rotation angles φ_p and φ_q are correctly accounted for. As previously elaborated for (20), the covariances between the equivalent copolarized channels ($q_m p_m$, $q_M p_M$) and the cross-polarized channels ($q_M p_m$, $q_m p_M$) are expected to be significantly lower than the copol intensities, although not concurrently null.

The remainder of this article will focus on analyzing and quantifying such rotations and assessing their implications in the design of a companion satellite mission.

V. METHODOLOGY

A. Metrics

The analysis is, at a first level, aimed at quantifying the rotations experienced by the different polarization orientations. On a deeper level, the objective is to evaluate whether a solid link can be established between the PTP–PRP defined in (25) and $(\mathbf{p}_M, \mathbf{q}_M)$ pair modeled in (26) and (27). Assessing the adherence of the bistatic scattering matrix to the reflection symmetry assumption in (31) is also of interest.

The link of (31) with (25) is evaluated numerically. A few tests have been proposed in literature to evaluate the degree of symmetry for both coherent [26] and incoherent [27] scatterers and retrieve the polarization rotation associated with the maximum symmetric component. Although these approaches could be in principle extended to our bistatic incoherent case study, the introduction of novel concepts and algorithms was deemed not beneficial to the clarity of this article. To estimate the degree of symmetry for an arbitrary polarization pair (p, q) and their orthogonal set $(p_\perp, q_\perp)$, we hence formulated the following straightforward metric:

$$\chi_{pq} = \frac{\left| \left\langle S_{pq} S_{pq_\perp}^* \right\rangle \right| + \left| \left\langle S_{pq} S_{p_\perp q}^* \right\rangle \right|}{2 \left(\sigma_{qp}^{(b)} + \sigma_{q_\perp p_\perp}^{(b)} \right)}$$
$$+ \frac{\left| \left\langle S_{p_\perp q_\perp} S_{pq_\perp}^* \right\rangle \right| + \left| \left\langle S_{p_\perp q_\perp} S_{p_\perp q}^* \right\rangle \right|}{2 \left(\sigma_{qp}^{(b)} + \sigma_{q_\perp p_\perp}^{(b)} \right)} \quad (32)$$

that directly relates the energy in the covariance terms off-diagonal to the power of the main channels in the covariance matrix diagonal. A perfectly symmetric and reciprocal scatterer shall be characterized by a minimum $\chi = 0$. For each transmit polarization p, the minimum value χ

$$\chi_p = \min_q (\chi_{pq}) \quad (33)$$

can be obtained, where the optimal receive polarization q remains implicit.

The degree of polarization (DoP) of the wave, describing the percentage of polarized power, is therefore also of interest in the analysis, albeit not addressed by specific modeling or expectations. Independently of the polarization basis, the DoP can then be computed as [28]

$$\text{DoP} = \frac{\sqrt{Q^2 + U^2 + V^2}}{I} \quad (34)$$

TABLE I

SUMMARY OF THE FOUR SCATTERING ESTIMATION APPROACHES ADOPTED AND OF THE STRATEGIES APPLIED TO DERIVE THE METRICS AND CONSEQUENTLY THE OPTIMAL POLARIZATIONS FROM THEIR OUTPUT. THE NOT AVAILABLE (NA) ENTRY CONVEYS THAT THE PARAMETER CANNOT BE CALCULATED

Approach	Output	Covariance calculation	PTP-PRP calculation	χ calculation
Kirchoff Approximation (KA)	$\vec{P}_1(p)$ in (8)	NA	Not considered	NA
Elfouhaily	$\vec{P}(p)$ in (7)	NA	Max of $|\vec{P}(p)|$. Exhaustive search in p	NA
Small Slope Approximation (SSA2)	covariance matrix	Output	Exhaustive search in p and q from (25)	Exhaustive search in q from (33)
Method of Moments (MoM)	$\vec{E}^s$ from surface realization	Statistics from 50 realizations	Exhaustive search in p and q from (25)	Exhaustive search in q from (33)

where I, Q, U, and V are the components of the Stokes vector [21]

$$\mathbf{g} = \begin{bmatrix} I \\ Q \\ U \\ V \end{bmatrix} = \begin{bmatrix} C_h + C_v \\ C_h - C_v \\ 2\mathcal{R}(C_x) \\ 2\mathcal{I}(C_x) \end{bmatrix} = \begin{bmatrix} I_H + I_V \\ I_H - I_V \\ I_{45°} - I_{-45°} \\ I_L - I_R \end{bmatrix} \quad (35)$$

that represents the covariance of the field after a projection on a Pauli basis, hence rephrasing the information in (13) in a more physically interpretable form. The field is fully polarized when $I = Q + U + V$, i.e., when only one component, linear, circular or, in general, elliptical, is present.

B. Full Covariance Field Simulation Approaches

Note that the first-order scattered field expression in (8) and the second-order supplement introduced in (9) do not carry the full covariance information. To evaluate (33) and (34) such information is, however, needed. To this purpose, two additional field calculation approaches have been therefore considered:

1) the first is the SSA2 method [17] that proposes an extension of the small-slope approximation approach [29] to the second-order Bragg scattering terms. This corrected the prediction of out-of-plane bistatic scattering for an arbitrary set of polarization indices and improved the modeling of cross-polarization scattering, heavily underestimated in the first-order approximation methods.

2) the second is a numerical field calculation based on the well-known MoM technique [30], [31]. The method shall in principle account for higher order field components as it provides a full-wave solution of the scattering problem. The heavy computational burden necessarily limits the size of the rough surface geometry. Several realizations of the random surface have to be therefore generated and processed. The second-order statistics of the field from each surface sample, after projection into the receiver set $(\hat{q}, \hat{q}_\perp)$, shall then be computed to derive the elements in (31). In this study, the statistics are based on an overall amount of 50 realizations. To prevent edge effects the incident wave amplitude has been tapered by a Gaussian window [32]. The 3-D geometries have been generated with a length of 15λ in each direction and a maximum polygon width of $\lambda/5$, where λ is the wavelength.

Differently from KA and Elfouhaily approximations in (8) and (7), these techniques show a dependency on the rough
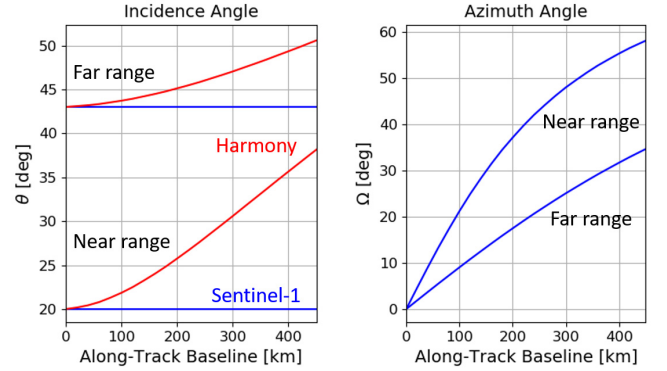

Fig. 6. Incidence (left) and azimuth (right) observation angles for Sentinel-1 and the next-generation Harmony companion. The near-range and far-range curves correspond to Sentinel-1 incidence angles of 20° and 44°, respectively.

surface spectrum. It must be therefore specified that the SSA2 technique has been applied to a rough sea surface generated by a wind with speed of 10 m/s and with same orientation of the ground range axis of the transmitting antenna. In the case of MoM simulation, the rough surface has been modeled by a Gaussian isotropic autocorrelation function with a correlation length of 3λ and a root mean square roughness of 0.5λ, corresponding to $kl \simeq 19$ and $k\sigma \simeq 3$. The type of information that is returned by each of the four scattering estimation approaches (KA, Elfouhaily, SSA2, and MoM) and the methods used to retrieve the principal polarizations, either maximizing (25) or minimizing (33), are summarized in Table I. Note that an exhaustive (brute-force) search is adopted for these last two metrics.

C. Application to a Bistatic Spaceborne Mission

We focus here on the specific bistatic configuration of a passive companion satellite following active spacecraft in the same orbit. The two satellites are distanced by a time delay dt, or equivalently, by an AT baseline $v_s dt$, where v_s is the speed of the two spacecrafts. The active satellite illuminates the ground at zero Doppler. The incidence plane, i.e., the plane formed by $\vec{k}_i$ and by the vertical polarization axis of the antenna, is therefore the plane orthogonal to the flying direction. The passive companion will consequently point to a location that is squinted with respect to its zero Doppler direction. In this particular configuration, the incidence angles for the transmitter do not match those for the receiver. These latter are intuitively a function of the ground range, AT baseline, and orbit height. The same dependency applies to the bistatic angle Ω, which shall not be considered as an independent
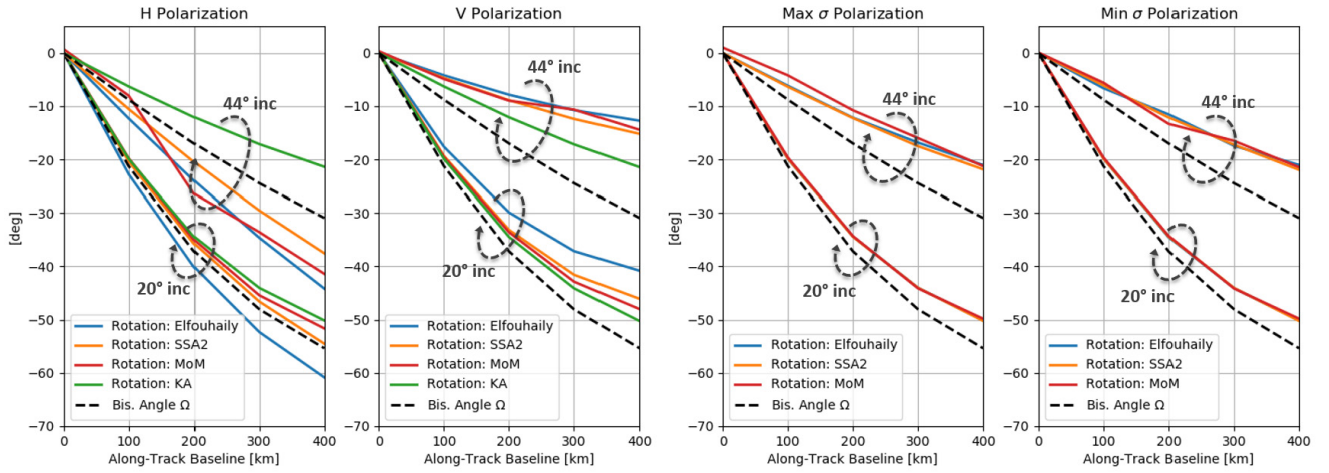
Fig. 7. Polarization rotation for a Sentinel-1 companion as a function of the AT baseline for two different incidence angles (20° and 44°). The panels cover four linear transmission modes with polarization unit vector oriented in different manners. From left to right: horizontal (H), vertical (V), thus describing the rotation $\triangle \psi$, maximum NRCS and minimum NRCS, describing the rotation $\triangle \psi_{P_m}$. The rotations, defined as in (11), are referred to the nominal H and V axes. The azimuth bistatic angle (black-dashed line) is reported in all the panels.

parameter. This work will conveniently adopt as reference configuration the Sentinel-1 height of 693 km. In such a way, the results will be readily applicable to the ESA Earth Explorer 10 Harmony mission. The bistatic angles for the Harmony as a function of the baseline and range are shown in Fig. 6. Note that in accordance with Fig. 1, the bistatic angles are positive since the companion satellite flies behind the main (right looking) spacecraft. A specular plot would have been produced by a companion flying ahead.

VI. RESULTS AND DISCUSSION

A. Principal Polarizations

For specular scattering scenarios, all the polarizations experience the same rotation $\triangle \psi$. Differently, for rough surface scattering, the polarization rotation is dependent on the polarization of the incidence wave as the Bragg and higher order scattering components have a significant impact on the scattered field orientation. The $(\hat{h}', \hat{v}')$ representation, largely adopted for specular scattering problems, shall be replaced by the principal polarizations representation, which accounts for the orientation of the surface with respect to the scattering plane. The rotation $\triangle \psi$ (defined in (29)) of the two principal sets, PTP_M-PRP_M and $\mathrm{PTP}_m - \mathrm{PRP}_m$, achieving, respectively, $\sigma_{\max}$ and $\sigma_{\min}$ in return, is expected to be the same, as the sets are orthogonal in receive and transmit. This is confirmed by the simulations from the three second-order field methods (Elfouhaily, SSA2, and MoM) shown in Fig. 7 (right panels). The simulations are illustrated for the two incidence angle extremes (20° and 44°) of the Sentinel-1 operation modes and for AT baselines ≤ 400 km. The rotations for the two nominal horizontal and vertical polarizations are reported in the first two panels of the figure. Note that the first-order KA rotations do not register significant difference between H and V, due to the inherent limitations in specular scattering approximation. The discrepancy with the estimates from the other approaches is then significant especially for large incidence angles. It is interesting to observe that KA rotations match the Bragg rotations for the principal polarizations shown in the two rightmost panels. This can be readily explained with the fact that the

maximum and minimum scattering intensities are expected when the supplemental field in (9) (associable to the first- and second-order Bragg processes) is aligned to the specular component in (8). The direction of the two field contributes the same in the case of maximum scattering (PTP_M, PRP_M), whereas it is the opposite in case of minimum scattering (PTP_m, PRP_m). A strong agreement on such alignment is found by SSA2, Elfouhaily, and MoM methods.

The orientations of the major and minor principal polarizations, i.e., (ψ_{P_M}, ψ_{q_M}), and (ψ_{P_m}, ψ_{q_m}), respectively, for 20° and 44° incidence angles are then represented in Fig. 8. The estimates from different methods are almost indistinguishable, with the exception of some residual uncertainty on MoM results for short baselines. The theoretical expectation, derived from (25), adheres perfectly to Elfouhaily estimates, and they stand within a 5° offset from SSA2 and MoM simulations. The model effectively accounts for the imbalance between PTP and PRP angles. The PRP is opposite in orientation direction with respect to the PTP, as the transmit and receive bases are intuitively symmetric with respect to the symmetry plane passing through the bisector (see Fig. 4); however, their absolute offsets from the nominal V and H are different. This imbalance is caused by the inclination of the symmetry plane with respect to scattering plane, or, identically, to the differences in the elevation angles of the incident and scattered waves.

A comprehensive polarimetric analysis is conducted for a single incidence angle of 36°, i.e., approximately at the center of the Sentinel-1 swath for the interferometric wide (IW) mode. Besides the polarization rotations, the panels in Fig. 9 report for all the polarization orientations in transmit: the received relative radar cross sections, the asymmetry defined in (33), and the degree of polarization in (34). These cross section panels reveal a good agreement between the second-order methods on the ratio $\sigma_{\min}/\sigma_{\max}$. SSA2 and MoM simulations produce, in particular, almost identical results, with higher estimates of the ratio when compared with the Elfouhaily method. Such differences in the radiometry are responsible for the discrepancies in polarization rotations. The
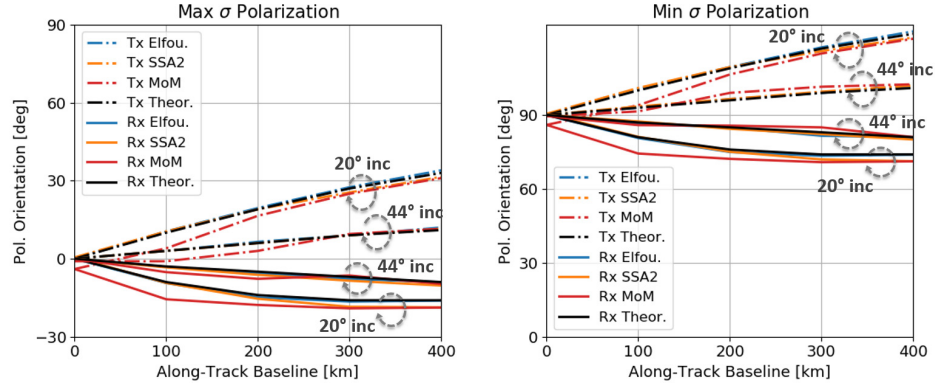
Fig. 8. Orientation of the maximum NRCS (left) and minimum NRCS (right) polarization pairs, i.e., (ψ_{p_M}, ψ_{q_M}), and (ψ_{p_m}, ψ_{q_m}), respectively, for a Sentinel-1 companion as a function of the AT baseline. The transmit (dash-dotted lines) and receive (solid lines) polarizations from the different techniques can be compared with the expressions in (26) and (27) (black-colored) for two different incidence angles, at near-range (20°) and far-range (44°).
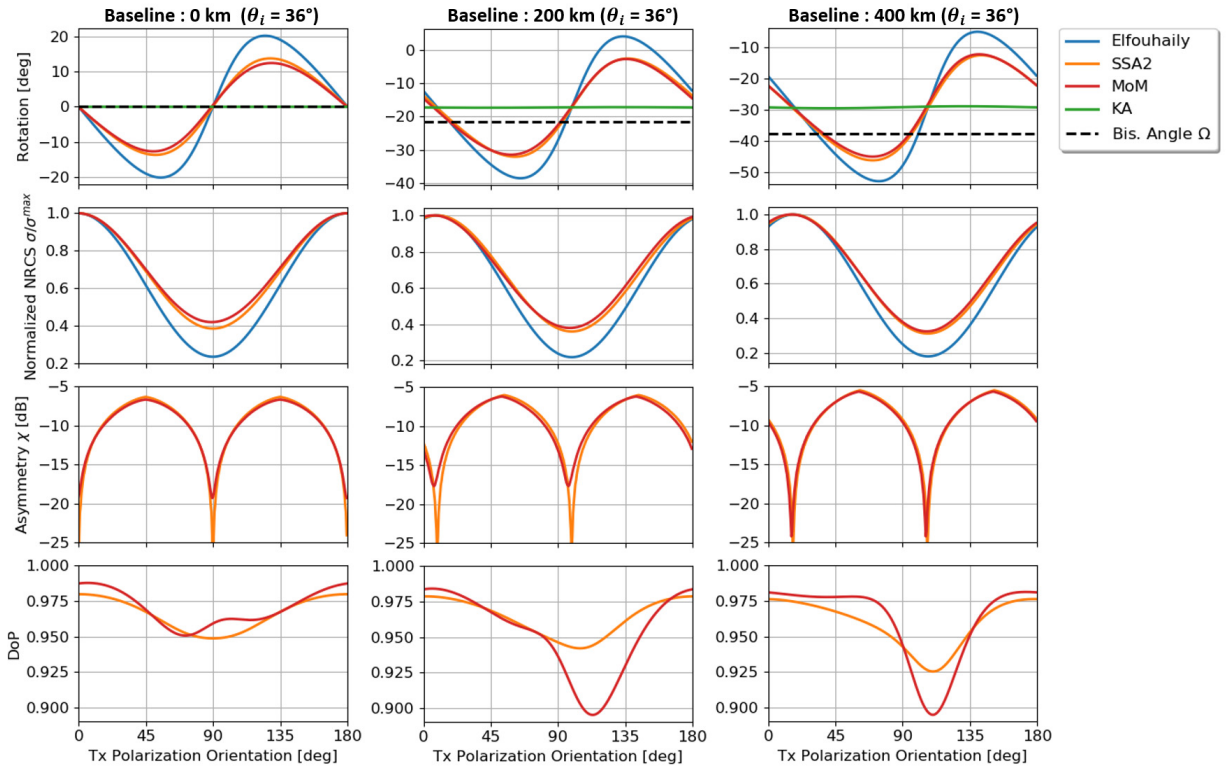

Fig. 9. Polarimetry overview for the Sentinel-1 companion at $\theta_i = 36°$. Polarization rotation (top graphs), normalized NRCS (second row graphs), asymmetry (third row graphs), and degree of polarization (bottom graphs) are estimated for all the linear polarizations in transmit ψ_i, with $\psi_i = 0$ representing the nominal V. The NRCS is evaluated for the receive polarization registering the maximum value.

panels also confirm that the first-order specular scattering provides consistent estimates only in correspondence of the principal polarizations. The asymmetry metric χ is also in line with the expectations, with a steep drop in correspondence of the two principal polarizations. Although the behavior of MoM and SSA2 is similar, the notch measured by MoM is less pronounced due to the finite number and width of the simulated geometries. The drop for nonnull baselines stands within the -20 to -25-dB range, due to the inclined symmetry plane and the consequent lack of the symmetries discussed in Section III and Appendix A. The two techniques present more evident differences on the degree of polarization, although they roughly share the same patterns. The fluctuations on the MoM

curves are attributable to the finite number of realizations. The depolarization is stronger for PTP$_m$ ($\sigma_{\min}$) component, whereas it is minimum for nominal vertical polarization (0°, 180° orientation). This implies that the unpolarized component of the Kirchhoff and Bragg scattering is relatively stronger for the principal polarization PTP$_m$ than for V. According to the simulations, the DoP also decreases with the bistatic angle.

B. Impact on Companion Mission Design

The effects of bistatic angles on the polarization orientation lead to further transmit and receive system considerations on the mission design. With regard to the receive antenna system, it becomes evident that a dual-polarization system is
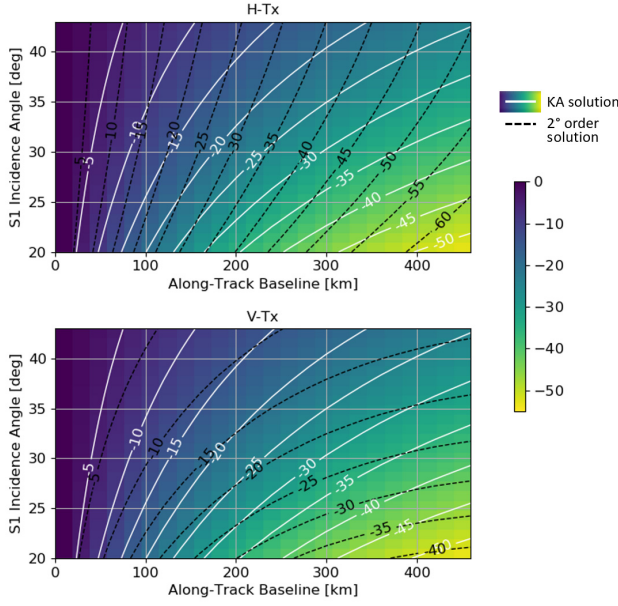
Fig. 10. Polarization rotation $\Delta\psi$ observed at the Harmony receiver for the active satellite transmitting in horizontal (upper panel) and vertical (lower panel) polarizations. The first-order and second-order field solutions are presented with solid and dashed contour lines, respectively.
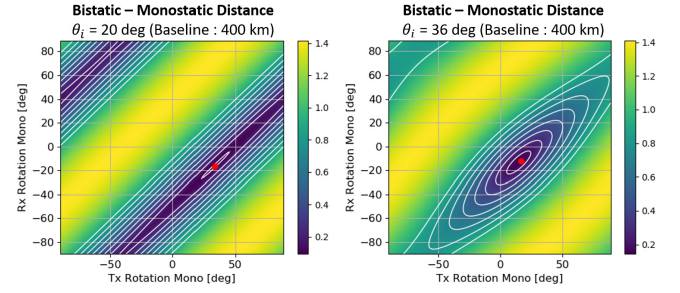

Fig. 11. Distance between the covariance matrix in a bistatic configuration, for the nominal H, V set, and that in a monostatic configuration, for a rotated polarization set in Tx (horizontal axis) and Rx (vertical axis). The distance has been computed with (37) on MoM simulations for two S1 incidence angles (20° and 36°). The red dot indicates the principal polarization angles φ_p and φ_q.

needed to optimally intercept the scattered power. In monostatic systems, the main advantage of dual-polarized receivers over single-polarized ones is to enable the exploitation of the cross-polarized scattering component that may bring independent information on the target. In bistatic systems the dual-polarized system is instead primarily required to match the polarization of the scattered field and avoid a partial loss of the scattered power. The orientation of this latter depends on the transmitted polarization but also on the angle of incidence and on the AT baseline. For the companion configuration in Fig. 6, the expected range of rotations over the Sentinel-1 swaths is illustrated in Fig. 10. The panels show that for large baselines (>300 km) and low incidence angles, the power intercepted by nominal cross-polarizations, VH and HV, is larger than the one in nominal copolarizations. This phenomenon is stronger for the H transmission mode, for which the 45° rotation threshold is reached for near-ranges of the Sentinel-1 IW swath.

A further reflection shall be conducted on the optimal linear polarization in transmission for bistatic systems. The results in Fig. 9 confirm that the maximum scattered power is achieved by the major principal polarization PTP_M, defined by (28). This represents therefore the best option for applications based on a single channel, such as SAR interferometry, and largely dependent on the SNR. Conversely, the transmission in nominal H and V could be favored by applications relying on polarimetric scattering decomposition, such as surface classification and bio-physical parameter retrieval. This readily follows from the observation that H and V can be equivalently represented through rotated polarizations:

$$\text{H}_{eq} - \text{Tx} : \begin{bmatrix} E^i_{p_m}(t) \\ E^i_{p_M}(t) \end{bmatrix} \propto \begin{bmatrix} \cos\varphi_p \\ -\sin\varphi_p \end{bmatrix}$$

$$\text{V}_{eq} - \text{Tx} : \begin{bmatrix} E^i_{p_m}(t) \\ E^i_{p_M}(t) \end{bmatrix} \propto \begin{bmatrix} \sin\varphi_p \\ \cos\varphi_p \end{bmatrix} \quad (36)$$

in the principal polarization basis $(\mathbf{p}_m, \mathbf{p}_M)$. The practical consequence of (36) and approximation in (31) is that the sensitivity to $\sigma^{(b)}_{q_m p_m}$, $\sigma^{(b)}_{q_M p_M}$, and $\rho^{(b)}$ would be enhanced for increasing angles φ_p at the expense of $\sigma^{(b)}_x$. Ideally, for $\varphi_p = \pi/4$, $(\text{PTP}_M, \text{PRP}_M)$ channel would then observe $\sigma^{(b)}_{q_M p_M} + \sigma^{(b)}_x$, whereas $(\text{PTP}_m, \text{PRP}_m)$ channel would measure $\sigma^{(b)}_{q_m p_m} + \sigma^{(b)}_x$.

C. Pseudo-Compact Equivalent

A connection with compact polarization modes can be established. It shall be hence recalled that compact modes, such as the transmission of a 45° rotated polarization, also denoted $\pi/4$-pol mode, have been promoted for their convenient polarimetric information content, as they represent a good surrogate for full polarimetry when some cross correlation assumptions can be applied [33], [34]. The operation in V or H in a bistatic configuration can therefore be compared, in terms of sensitivity to target parameters, with an equivalent monostatic mode with orientation φ_p in transmission and wave vector corresponding to the bisector $\vec{k}_{i,s}/2$ in (10). We will call this pseudo-compact mode as φ_p-pol mode. The angle φ_p corresponds to the characteristic orientation, ψ_{p_m}, of PTP_m, which varies across the swath, as shown in Fig. 12. The equivalent compact modes do not reach the extent of $\pi/4$-pol modes. For the IW swath, a $\pi/10$-pol equivalent mode is indeed expected at near-ranges for a 300-km baseline. It shall be nevertheless remarked that the zero-squint illumination of Sentinel-1 is particularly convenient in this respect, as it determines a higher deviation from V for the PTP rather than for the PRP. This equivalence speculation was further tested by measuring the distance between the covariance matrix $\mathbf{C}(\vec{k}_i, \vec{k}_s)$ of the bistatic configuration in nominal H, V and the covariance matrix $\mathbf{C}_{\varphi_p, \varphi_q}(\vec{k}_{i,s}/2, \vec{k}_{i,s}/2)$ of the monostatic equivalent for all the rotation combinations (φ_i, φ_j) in Tx and Rx. The Frobenius norm of the difference

$$\left\| \frac{\mathbf{C}(\vec{k}_i, \vec{k}_s)}{\|\mathbf{C}(\vec{k}_i, \vec{k}_s)\|} - \frac{\mathbf{C}_{\varphi_i, \varphi_j}(\vec{k}_{i,s}/2, \vec{k}_{i,s}/2)}{\|\mathbf{C}_{\varphi_i, \varphi_j}(\vec{k}_{i,s}/2, \vec{k}_{i,s}/2)\|} \right\|_F \quad (37)$$

was used to measure the similarity, with the matrices being normalized by their determinant. The two scattering simulations in Fig. 11, performed with MoM for a baseline of
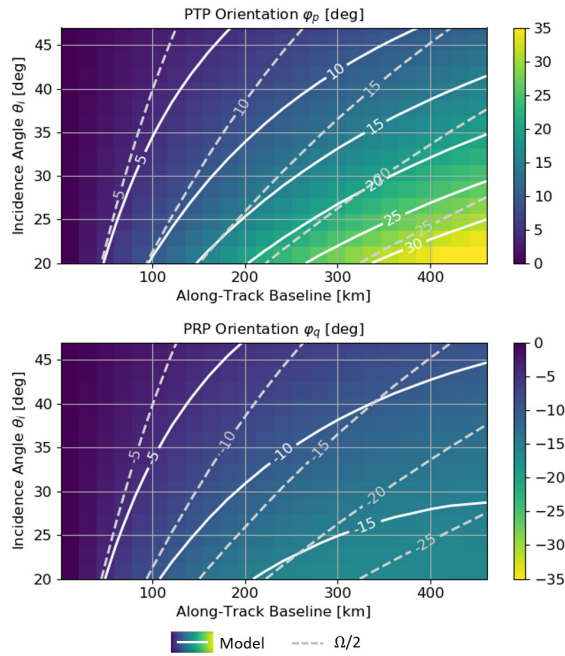
Fig. 12. Principal polarization orientations in transmit (upper panel) and receive (lower panel) for different Harmony AT baselines and Sentinel-1 incidence angles. The solid contour lines are compared with the halved bistatic angle $\Omega/2$ illustrated with dashed lines.

400 km, confirm that the mode described by the rotations in (26) and (27) achieves the best similarity.

The approximate reflection symmetry in (31), when adopting the principal polarization bases, has a potential impact on the system calibration strategies. It is well-known that distributed targets are exploited in monostatic acquisitions for complementing man-made calibrators on assessing the polarimetric quality of the system. The crosstalk and power imbalance in the bistatic receiver could then be similarly monitored and adjusted using rough surfaces and exploiting the (28) condition. However, the nonnull correlation coefficients $\langle S_{q_l p_m} S_{q_i p_i}^* \rangle_{l \neq m}$, the lack of reciprocity, $\sigma_{q_m p_M}^{(b)} \neq \sigma_{q_M p_n}^{(b)}$, and the relatively weak scattering of rough surfaces suggest to be cautious on the accuracy achievable for the cross-talks and imbalances' estimation. Our investigation provides only a rough empirical assessment on the validity of such equivalence and cannot be considered highly representative for the large variety of scattering covariances of real surfaces. Such potential opportunity needs therefore to be carefully assessed with real data. Note, in conclusion, that the application of the elaborated theory to other types of distributed scatterers, such as random or oriented volume scatterers, shall be in general avoided.

D. Note on Scattering Mechanisms Separability

In the previous discussions, we exploited different first- and second-order model approximations to rough-surface scattering. We can also see them as representing different scatterer types or scattering mechanisms. For example, for oceans, KA is valid for specular scattering associated with localized steep slopes caused by high wind [35], [36], while the second-order approximation includes what is commonly recognized as Bragg scattering. The first row in Fig. 9 illustrates clearly how different scattering mechanisms result in different magnitude and polarization inclination of the scattered signals, except when the polarization of the incident wave corresponds to one of the principal polarizations, a case where the rotation shall be zero despite the considered curve. In the monostatic case, we observe that the variation in the rotation angles (i.e., the separation among curves of different colors) is maximized for transmit polarization angles around 35°–40° at the center of the Sentinel-1 swath, i.e., for a 36° incidence. For the 400-km baseline case, we see that the polarimetric separability (i.e., separation among the curves) is maximized for Tx polarization angles around −20° or 50°. The second option is interesting as it comes close to the compact-pol transmission concept. However, given that for Harmony, being a companion of Sentinel-1, we can only choose between a 0° (H) and 90° (V) Tx polarizations, it is worth noting that at 0° this separability is reasonably near the maximum.

VII. Conclusion

The study shed light on the orientation and the second-order properties of the scattered field from rough surfaces in a companion SAR mission geometry. The use of the nominal ground-aligned H and V polarizations is questioned, as in bistatic system they are not aligned with the dominant orientation of the natural targets. A new set of characteristic linear polarizations in transmit and receive was proposed, and a simple geometric model for their orientation was derived. Such polarizations, herewith named PTP and PRP, were more specifically defined as the sets that provide the maximum ($\text{PTP}_M - \text{PRP}_M$) and minimum ($\text{PTP}_m - \text{PRP}_m$) power at the receiver, respectively. The associated basis rotations, φ_p in transmit and φ_q in receive, were linked to the inclination of the rough surface symmetry plane with respect to the scattering plane. The first is the plane described by the average rough surface normal and the bistatic angle (transmitter–target–receiver) bisector. Although such plane represents an effective symmetry plane only in the case of isotropic rough surfaces, a good adherence to the model is also expected for weakly anisotropic surfaces, such as the sea surface in mild wind conditions. A 2° to 5° maximum departure from the PTP and PRP rotations was confirmed through simulations from multiple second-order scattering models, which include the Elfouhaily method and the numerical MoM, based on isotropic surface models, and the second-order small-slope approximation, simulating an anisotropic sea spectrum configuration.

Through the synthetic data, it was verified that the rotated PTP–PRP basis minimizes the covariance between the copolarized and cross-polarized channels, which record intensities −15 to −25 dB lower than the power in copolarized channels. Although the reflection symmetry conditions (demanding null correlations) are not perfectly met, an equivalence between the actual bistatic scattering and an equivalent monostatic scattering, in the principal polarization basis, can be established in terms of polarimetric sensitivity to target properties. This allows to compare the transmission of H and V in a bistatic system with the transmission of a polarization rotated by φ_p and $\varphi_p + \pi/2$ from an equivalent monostatic system.

The resulting effect is a potential enhancement in the target discrimination capability of a companion mission when combined with the monostatic acquisitions. It was assessed that the angle φ_p varies from a few degrees for short baselines, or high incidence angles, to 20–25° for baselines of 300 km and low incidence angles ($<30°$). A companion mission with large baseline, such as the Earth Explorer 10 Harmony candidate, experiences therefore a diversity in the polarimetric sensitivity across the swath.

It was further observed that the principal polarizations are characterized by a substantial alignment between specular scattering and second- (or higher) order Bragg scattering components. The direction of the two components is the same for the strongest return polarization ($\text{PTP}_M - \text{PRP}_M$), whereas it is opposite for the weakest return one ($\text{PTP}_m - \text{PRP}_m$). The interaction of these two components determines a larger polarization rotation and a lower scattered intensity for a transmission in H with respect to V. Although the use of the vertical polarization would therefore be more convenient for SNR-driven applications, the larger rotation of H provides better separability potential between scattering mechanisms, e.g., for ocean applications. In either case, it can be concluded that a bistatic systems shall not rely on a single traditional channel HH or VV in receive but they shall seek for the optimal receive polarization, provided their dual-polarimetric capabilities.

APPENDIX A
ANALYSIS OF THE REFLECTION SYMMETRIES

Let consider a coherent target with a symmetry plane corresponding to the bisector plane. This latter is defined as the plane formed by the bisector $\hat{s} + \hat{i}$ and the scattering plane normal $\hat{s} \times \hat{i}/|\hat{s} \times \hat{i}|$. Suppose then that the reference horizontal axes of the transmit and receive polarization planes lie on the scattering plane and that consequently for the vertical polarization $\hat{v}_i = \hat{v}_s = \hat{i} \times \hat{s}/|\hat{i} \times \hat{s}|$ holds. Using the backward scattering alignment (BSA) convention, the horizontal polarizations in transmit and receive are defined, respectively, by $\hat{h}_i = \hat{i} \times \hat{v}_i$ and $\hat{h}_s = \hat{s}_s \times \hat{v}$. To derive the effect of the symmetry on the scattering matrix, we shall first observe that in such symmetric scenario we can exchange transmitter and receiver, and thus the following relationships hold:

$$S_{hh}(\hat{i}, \hat{s}) = S_{hh}(\hat{s}, \hat{i}) \tag{38}$$
$$S_{vv}(\hat{i}, \hat{s}) = S_{vv}(\hat{s}, \hat{i}) \tag{39}$$
$$S_{hv}(\hat{i}, \hat{s}) = -S_{hv}(\hat{s}, \hat{i}) \tag{40}$$
$$S_{vh}(\hat{i}, \hat{s}) = -S_{vh}(\hat{s}, \hat{i}) \tag{41}$$

where the sign inversion for the cross-polarized terms is due to BSA convention, as the symmetry is achieved by inverting the direction of the horizontal received field component with respect to the horizontal unit vector $\hat{h}_s$. By further accounting for the scattering reciprocity conditions

$$S_{hv}(\hat{i}, \hat{s}) = S_{vh}(\hat{s}, \hat{i}) \tag{42}$$
$$S_{vh}(\hat{i}, \hat{s}) = S_{hv}(\hat{s}, \hat{i}) \tag{43}$$

valid for all the scattering scenarios, and by combining (40-41) with (42-43), the fundamental property

$$S_{hv}(\hat{i}, \hat{s}) = -S_{vh}(\hat{i}, \hat{s}) \tag{44}$$

for the geometry mirroring with respect to the bisector plane is obtained. Note that in the monostatic case, i.e., a target symmetry with respect to the incidence plane, (44) leads to $S_{hv} = S_{vh} = 0$. The symmetry problems can also treated by accounting for an adjoint term in the scattering matrix. In the case of bisector mirroring, the target can be represented by the superposition of a generic nonsymmetric component $\mathbf{S}'$ and by this adjoint (mirrored) component $\mathbf{S}''$, defined as

$$\mathbf{S} = \mathbf{S}' + \mathbf{S}'' = \begin{bmatrix} a & b \\ c & d \end{bmatrix} + \begin{bmatrix} a & -c \\ -b & d \end{bmatrix}. \tag{45}$$

The symmetry problem for incoherent targets is an extension of the coherent case, which implies to consider an ensemble of scatterers. By referring to (45), let us consider two distinct populations of scatterers $\mathbf{S}'$ and $\mathbf{S}''$ with their elements $\{a', b', c', d'\}$ and $\{a'', b'', c'', d''\}$, which shall now be interpreted in a stochastic sense, i.e., it is implied that the first- and second-order moments are the same. The properties will hence be derived for the second-order statistics

$$\gamma_{ijij} = \langle S_{ij} S_{ij}^* \rangle = \frac{\langle S_{ij}' S_{ij}'^* \rangle + \langle S_{ij}'' S_{ij}''^* \rangle}{2}$$

$$\gamma_{ijji} = \langle S_{ij} S_{ji}^* \rangle = \frac{\langle S_{ij}' S_{ji}'^* \rangle + \langle S_{ij}'' S_{ji}''^* \rangle}{2}$$

with $i, j = \{h, v\}$. The first equation represents the average power of each polarization and the second equation the cross-covariance terms. It is readily shown that the amplitude and sign constrains between S_{hv} and S_{vh} further reduce the degrees of freedom in the covariance elements as they lead to

$$\gamma_{hvhv} = \frac{\langle |c|^2 \rangle + \langle |b|^2 \rangle}{2} = \gamma_{vhvh}$$
$$\gamma_{hvhh} = \frac{\langle ba^* \rangle - \langle ca^* \rangle}{2} = -\gamma_{vhhh}$$
$$\gamma_{hvvv} = \frac{\langle bd^* \rangle - \langle cd^* \rangle}{2} = -\gamma_{vhvv}. \tag{46}$$

The covariance term between the cross-polarizations instead takes the real-valued expression

$$\gamma_{hvvh} = \frac{\langle bc^* + cb^* \rangle}{2} = \langle \mathcal{R}\{cb^*\} \rangle \tag{47}$$

that cannot be further developed, since, in a generic mirroring problem, no additional relationships can be established between c and b. More simplifications are expected in case of scattering reciprocity. A reciprocity scenario implies the scattering invariance with respect to the rotation of the target by π about the bisector. In such a case, we would observe in the coherent case

$$\mathbf{S} = \mathbf{S}' + \mathbf{S}'' = \begin{bmatrix} a & b \\ c & d \end{bmatrix} + \begin{bmatrix} a & c \\ b & d \end{bmatrix} \tag{48}$$

so that $S_{hv} = S_{vh}$,, whereas for incoherent scattering we can readily derive

$$\gamma_{hvhv} = \gamma_{vhvh}$$

$$\gamma_{hvhh} = \gamma_{vhhh}$$
$$\gamma_{hvvv} = \gamma_{vhvv} \qquad (49)$$

and for γ_{hvvh} the same expression in (47) still applies. By combining both reciprocity and bisector mirroring, and thus to satisfy both (46) and (49), we would finally achieve a covariance expression similar to the reflection symmetry in monostatic case

$$\mathbf{C} = \begin{bmatrix} \gamma_{hhhh} & 0 & 0 & \gamma_{vvhh}^* \\ 0 & \gamma_{vhvh} & \gamma_{hvvh}^* & 0 \\ 0 & \gamma_{hvvh} & \gamma_{hvhv} & 0 \\ \gamma_{vvhh} & 0 & 0 & \gamma_{vvvv} \end{bmatrix} \qquad (50)$$

where no additional constraints on γ_{vvhh} and γ_{vhvh} can be generally formulated. It can finally be noted that the condition $\gamma_{hvvh} = \gamma_{hvhv} = \gamma_{vhvh}$ is achieved only in a scenario where every element in the population satisfies the scattering reciprocity, in a coherent sense. This is for instance the case of monostatic configurations.

Acknowledgment

The authors would like to thank Dr. Alexander Voronovich for sharing his implementation of the SSA-2 model and Andreas Theodosiou for writing a Python wrapper to run the model in the particular geometry of Harmony. The authors would also like to thank Dr. Marcel Kleinherenbrink for the discussions on the work at its early stage and Dr. Bertrand Charpron for sharing his insights and, in particular, for insisting that we follow the work by Elfouhaily *et al.* [1].

References

[1] T. Elfouhaily, D. R. Thompson, B. Chapron, and D. Vandemark, "A new bistatic model for electromagnetic scattering from perfectly conducting random surfaces," *Waves Random Media*, vol. 9, pp. 281–294, Jul. 1999.

[2] M. Antoniou and M. Cherniakov, "GNSS-based bistatic SAR: A signal processing view," *EURASIP J. Adv. Signal Process.*, vol. 2013, no. 1, pp. 1–16, May 2013.

[3] C. Ruf *et al.*, "In-orbit performance of the constellation of CYGNSS hurricane satellites," *Bull. Amer. Meteorolog. Soc.*, vol. 100, no. 10, pp. 2009–2023, Oct. 2019.

[4] M. J. Unwin *et al.*, "An introduction to the HydroGNSS GNSS reflectometry remote sensing mission," *IEEE J. Sel. Topics Appl. Earth Observ. Remote Sens.*, vol. 14, pp. 6987–6999, 2021.

[5] D. Comite and N. Pierdicca, "Decorrelation of the near-specular land scattering in bistatic radar systems," *IEEE Trans. Geosci. Remote Sens.*, vol. 60, pp. 1–13, 2022.

[6] G. Krieger *et al.*, "TanDEM-X: A satellite formation for high-resolution SAR interferometry," *IEEE Trans. Geosci. Remote Sens.*, vol. 45, no. 11, pp. 3317–3341, Nov. 2007.

[7] G. Krieger *et al.*, "The tandem-L mission proposal: Monitoring Earth's dynamics with high resolution SAR interferometry," in *Proc. IEEE Radar Conf.*, May 2009, pp. 1–6.

[8] N. Gebert, B. C. Dominguez, M. W. J. Davidson, M. D. Martin, and P. Silvestrin, "SAOCOM-CS—A passive companion to SAOCOM for single-pass L-band SAR interferometry," in *Proc. EUSAR 10th Eur. Conf. Synth. Aperture Radar*, Jun. 2014, pp. 1–4.

[9] P. Lopez-Dekker *et al.*, "Companion SAR constellations for single-pass interferometric applications: The SESAME mission," in *Proc. IEEE Int. Geosci. Remote Sens. Symp. (IGARSS)*, Jul. 2017, pp. 119–122.

[10] P. Lopez-Dekker, H. Rott, P. Prats-Iraola, B. Chapron, K. Scipal, and E. D. Witte, "Harmony: An Earth explorer 10 mission candidate to observe land, ice, and ocean surface dynamics," in *Proc. IEEE Int. Geosci. Remote Sens. Symp.*, Jul. 2019, pp. 8381–8384.

[11] D. Comite and N. Pierdicca, "Bistatic radar systems at large baselines for ocean observation," *IEEE Trans. Geosci. Remote Sens.*, vol. 56, no. 3, pp. 1816–1828, Mar. 2018.

[12] J. R. Huynen, "Physical reality and mathematical process in radar polarimetry," in *Proc. 7th Int. Conf. Antennas Propag. (ICAP)*, vol. 1, Apr. 1991, pp. 257–261.

[13] A.-L. Germond, "Foundations of bistatic radar polarimetry theory," in *Proc. Radar Syst. (RADAR)*, Oct. 1997, pp. 833–837.

[14] N. Trouve, E. Colin-Koeniguer, P. Fargette, and A. De Martino, "Influence of geometrical configurations and polarization basis definitions on the analysis of bistatic polarimetric measurements," *IEEE Trans. Geosci. Remote Sens.*, vol. 49, no. 6, pp. 2238–2250, Jun. 2011.

[15] C. Titin-Schnaider, "Physical meaning of bistatic polarimetric parameters," *IEEE Trans. Geosci. Remote Sens.*, vol. 48, no. 5, pp. 2349–2356, May 2010.

[16] S. V. Nghiem, S. H. Yueh, R. Kwok, and F. K. Li, "Symmetry properties in polarimetric remote sensing," *Radio Sci.*, vol. 27, no. 5, pp. 693–711, Sep./Oct. 1992.

[17] A. G. Voronovich and V. U. Zavorotny, "Full-polarization modeling of monostatic and bistatic radar scattering from a rough sea surface," *IEEE Trans. Antennas Propag.*, vol. 62, no. 3, pp. 1362–1371, Mar. 2014.

[18] J. T. Johnson, C. J. Baker, G. E. Smith, K. L. Bell, and M. Rangaswamy, "The monostatic-bistatic equivalence theorem and bistatic radar clutter," in *Proc. 11th Eur. Radar Conf.*, Oct. 2014, pp. 105–108.

[19] R. Torres *et al.*, "GMES Sentinel-1 mission," *Remote Sens. Environ.*, vol. 120, pp. 9–24, May 2012. [Online]. Available: http://www.sciencedirect.com/science/article/pii/S0034425712000600

[20] A. Poggio and E. Miller, "Integral equation solutions of three-dimensional scattering problems," in *Computer Techniques for Electromagnetics* (International Series of Monographs in Electrical Engineering), R. Mittra, Ed. New York, NY, USA: Pergamon, 1973, pp. 159–264.

[21] E. Collett, *Field Guide to Polarization*, vol. FG05. Bellingham, WA, USA: SPIE, 2005.

[22] L. Tsang, J. A. Kong, and K.-H. Ding, *Scattering of Electromagnetic Waves: Theories and Applications*. Hoboken, NJ, USA: Wiley, 2004.

[23] S. H. Yueh, R. Kwok, and S. V. Nghiem, "Polarimetric scattering and emission properties of targets with reflection symmetry," *Radio Sci.*, vol. 29, no. 6, pp. 1409–1420, Nov./Dec. 1994.

[24] S. R. Cloude, "On the status of bistatic polarimetry theory," in *Proc. IEEE Int. Geosci. Remote Sens. Symp. (IGARSS)*, vol. 3, Jul. 2005, pp. 2003–2006.

[25] Y. Wang, T. L. Ainsworth, and J.-S. Lee, "On the geometrical dependency of the polarimetric bistatic SAR observation," in *Proc. IEEE Int. Geosci. Remote Sens. Symp.*, Jul. 2019, pp. 4935–4938.

[26] C. Titin-Schnaider, "Characterization and recognition of bistatic polarimetric mechanisms," *IEEE Trans. Geosci. Remote Sens.*, vol. 51, no. 3, pp. 1755–1774, Mar. 2013.

[27] S. Zwieback and I. Hajnsek, "Statistical tests for symmetries in polarimetric scattering coherency matrices," *IEEE Geosci. Remote Sens. Lett.*, vol. 11, no. 1, pp. 308–312, Jan. 2014.

[28] R. C. Jones, "A new calculus for the treatment of optical systems v. A more general formulation, and description of another calculus," *J. Opt. Soc. Amer.*, vol. 37, no. 2, pp. 107–110, Feb. 1947. [Online]. Available: http://www.osapublishing.org/abstract.cfm?URI=josa-37-2-107

[29] A. G. Voronovich, "Small-slope approximation for electromagnetic wave scattering at a rough interface of two dielectric half-spaces," *Waves Random Media*, vol. 4, no. 3, pp. 337–367, Jul. 1994.

[30] K. F. Warnick and W. C. Chew, "Numerical simulation methods for rough surface scattering," *Waves Random Media*, vol. 11, no. 1, pp. R1–R30, Jan. 2001.

[31] A. Ishimaru, J. S. Chen, P. Phu, and K. Yoshitomi, "Numerical, analytical, and experimental studies of scattering from very rough surfaces and backscattering enhancement," *Waves Random Media*, vol. 1, no. 3, pp. S91–S107, Jul. 1991.

[32] A. K. Fung and M. F. Chen, "Numerical simulation of scattering from simple and composite random surfaces," *J. Opt. Soc. Amer. A, Opt. Image Sci.*, vol. 2, no. 12, pp. 2274–2284, Dec. 1985. [Online]. Available: http://josaa.osa.org/abstract.cfm?URI=josaa-2-12-2274

[33] R. K. Raney, "Hybrid-polarity SAR architecture," *IEEE Trans. Geosci. Remote Sens.*, vol. 45, no. 11, pp. 3397–3404, Nov. 2007.

[34] M. E. Nord, T. L. Ainsworth, J.-S. Lee, and N. J. S. Stacy, "Comparison of compact polarimetric synthetic aperture radar modes," *IEEE Trans. Geosci. Remote Sens.*, vol. 47, no. 1, pp. 174–188, Jan. 2009.

[35] V. N. Kudryavtsev, B. Chapron, A. G. Myasoedov, F. Collard, and J. A. Johannessen, "On dual co-polarized SAR measurements of the ocean surface," *IEEE Geosci. Remote Sens. Lett.*, vol. 10, no. 4, pp. 761–765, Jul. 2013.

[36] V. Kudryavtsev, I. Kozlov, B. Chapron, and J. A. Johannessen, "Quad-polarization SAR features of ocean currents," *J. Geophys. Res. Oceans*, vol. 119, no. 9, pp. 6046–6065, Sep. 2014, doi: 10.1002/2014JC010173.

Lorenzo Iannini (Member, IEEE) received the master's degree in telecommunications engineering and the Ph.D. degree in defending a dissertation on the polarimetric calibration of synthetic aperture radars (SARs) from the Politecnico di Milano, Milan, Italy, in 2008 and 2013, respectively.

He continued his research in the Geoscience and Remote Sensing Department, Delft University of Technology, Delft, The Netherlands. During his ten years' experience in Milano and Delft, he was engaged in multiple project initiatives aimed at devising radar processing algorithms for land cover monitoring and evaluating spaceborne SAR systems performance. He is providing science support to the future Copernicus SAR Missions at the European Space Agency.

Davide Comite (Senior Member, IEEE) received the master's degree *(cum laude)* in telecommunications engineering and the Ph.D. degree in electromagnetics and mathematical models for engineering from Sapienza University, Rome, Italy, in 2011 and 2015, respectively.

He is a Tenure Track Assistant Professor with Sapienza University. He was a Visiting Ph.D. Student with the Institute of Electronics and Telecommunications of Rennes, University of Rennes 1, Rennes, France, in 2014, and a Post-Doctoral Researcher with the Center of Advanced Communications, Villanova University, PA, USA, in 2015. His scientific interests involve Earth observation, remote sensing, the study of scattering from natural surfaces, GNSS reflectometry over land, and radar altimetry for biomass estimation. He is also interested in the study and design of microwaves and millimeter-wave antennas, antenna arrays, and leaky-wave antennas, as well as in the generation of nondiffracting waves and pulses. In 2019, 2020, and 2021, the IEEE Antennas and Propagation Society recognized Davide as an Outstanding Reviewer for the IEEE Transaction on Antennas and Propagation.

Dr. Comite was awarded as the Best Reviewer for the IEEE JOURNAL OF SELECTED TOPICS IN APPLIED EARTH OBSERVATION AND REMOTE SENSING in 2020. He serves as a Reviewer for several international journals. He is an Associate Editor of the *Journal of Engineering and the Microwaves, Antennas and Propagation* by the Institution of Engineering and Technology (IET). He is also an Associate Editor of IEEE ACCESS and the EurAAP Journal of *Reviews of Electromagnetics*, and the IEEE JOURNAL OF SELECTED TOPICS IN APPLIED EARTH OBSERVATION AND REMOTE SENSING. He has been leading the GNSS-R Working Group of the GRSS MIRS Technical Committee since January 2021. He is an URSI Senior Member.

Nazzareno Pierdicca (Senior Member, IEEE) received the Laurea (Doctor's) degree *(cum laude)* in electronic engineering from the University La Sapienza of Rome, Rome, Italy, in 1981.

From 1978 to 1982, he worked with the Italian Agency for Alternative Energy (ENEA). From 1982 to 1990, he has been working with Telespazio, Rome, Italy, in the Remote Sensing Division. In November 1990, he joined the Department of Information Engineering, Electronics and Telecommunications, Sapienza University, Rome. He is a Full Professor and teaches remote sensing, antenna, and electromagnetic fields within the Faculty of Engineering. His research interests include electromagnetic scattering and emission models for sea and bare soil surfaces and their inversion, microwave radiometry of the atmosphere, radar land applications, and GNSS reflectometry. He is a past Chairperson of the GRSS Central Italy Chapter and the Chair of the GRSS MIRS Technical Committee.

Paco Lopez-Dekker (Senior Member, IEEE) was born in Nijmegen, The Netherlands, in 1972. He received the Ingeniero degree in telecommunication engineering from the Universitat Politècnica de Catalunya (UPC), Barcelona, Spain, in 1997, the M.S. degree in electrical and computer engineering from the University of California, Irvine, CA, USA, in 1998, under the Balsells Fellowship, and the Ph.D. degree in clear-air imaging radar systems to study the atmospheric boundary layer from the University of Massachusetts, Amherst, MA, USA, in 2003.

In 2003, he joined Starlab Barcelona, where he worked on the development of GNSS-R sensors and techniques. From 2004 to 2006, he was a Visiting Professor with the Department of Telecommunications and Systems Engineering, Universitat Autonoma de Barcelona. In March 2006, he was awarded a Ramon y Cajal Grant to conduct pioneering research on bistatic synthetic aperture radar (SAR) at Remote Sensing Laboratory, UPC. At the university, he taught courses on signals and systems, signal processing, communications systems and radiation, and guided waves. Between November 2009 and August 2016, he led the SAR Missions Group at the Microwaves and Radar Institute, German Aerospace Center, Wessling, Germany. Since September 2016, he has been an Associate Professor with the Geoscience and Remote Sensing Department, Faculty of Civil Engineering and Geosciences. He has been deeply involved in several radar mission proposals, and is the Lead Investigator of the Harmony ESA Earth Explorer 10 Mission candidate. He has coauthored 50 peer-reviewed journal articles and more than 100 conference contributions in a broad range of topics related to radar remote sensing.